Structural, electronic, elastic, power, and transport properties of β-Ga_2O_3 from first principles

Samuel Poncé[1,2,*] and Feliciano Giustino[3,4,2,†]

[1]*Theory and Simulation of Materials (THEOS), École Polytechnique Fédérale de Lausanne, CH-1015 Lausanne, Switzerland*
[2]*Department of Materials, University of Oxford, Parks Road, Oxford OX1 3PH, United Kingdom*
[3]*Oden Institute for Computational Engineering and Sciences, The University of Texas at Austin, Austin, Texas 78712, USA*
[4]*Department of Physics, The University of Texas at Austin, Austin, Texas 78712, USA*

(Received 5 May 2020; accepted 24 June 2020; published 20 July 2020)

We investigate the structural, electronic, vibrational, power, and transport properties of the β allotrope of Ga_2O_3 from first principles. We find phonon frequencies and elastic constants that reproduce the correct band ordering, in agreement with experiment. We use the Boltzmann transport equation to compute the intrinsic electron and hole drift mobility and obtain room-temperature values of 258 and 1.2 cm^2/Vs, respectively, as well as 6300 and 13 cm^2/Vs at 100 K. Through a spectral decomposition of the scattering contribution to the inverse mobility, we find that multiple longitudinal-optical modes of B_u symmetry are responsible for the electron mobility of β-Ga_2O_3 but that many acoustic modes also contribute, making it essential to include all scattering processes in the calculations. Using the von Hippel low-energy criterion, we computed the breakdown field to be 5.8 MV/cm at room temperature, yielding a Baliga figure of merit of 1250 with respect to silicon, ideal for high-power electronics. This work presents a general framework to predictively investigate novel high-power electronic materials.

DOI: 10.1103/PhysRevResearch.2.033102

I. INTRODUCTION

The β allotrope of Ga_2O_3 has attracted some attention as an ultrawide-band-gap transparent semiconducting oxide [1]. As a consequence of its large band gap, β-Ga_2O_3 possesses a very high breakdown electric field of 8 MV/cm [2] and a large Baliga figure of merit (BFOM) [3], which makes it a promising alternative to GaN and SiC for high-power electronics [4,5]. In addition, it can be synthesized by the melt-growth method, which allows for low-cost and large-scale production [6,7]. Its electronic and optical properties also make it a good candidate for UV transparent conducting oxide (TCO) [8,9].

One property of β-Ga_2O_3 that makes it so attractive is its high carrier mobility for a material with such a wide band gap. The electron mobility of β-Ga_2O_3 has been studied more extensively than the hole mobility due to experimental interest and the fact the hole mobility is two orders of magnitude smaller. Given the promise offered by β-Ga_2O_3, it is surprising that many basic properties have not been investigated in detail. From a theoretical perspective, this might be due to the fact that β-Ga_2O_3 has a 10-atom primitive cell, which makes first-principles calculations in this material more challenging than for standard tetrahedral semiconductors. In particular, the shape of the conduction band was not well understood until recently. Indeed, Ueda *et al.* [10] measured a strong anisotropy of the conduction-band effective mass. However, since then many experiments and theoretical studies indicated that the conduction band is nearly isotropic [6,11–17]. Another question relates to the relative importance of nonpolar optical-phonon, polar optical-phonon, and ionized-impurity scattering at room temperature. Initially it was thought that the dominant scattering mechanism in β-Ga_2O_3 was due to nonpolar optical phonons with a large deformation potential of 4×10^9 eV/cm [18]. However, Ghosh and Singisetti [19] identified a longitudinal-optical phonon mode with energy around 21 meV as the dominant mechanism in the mobility of β-Ga_2O_3, and this finding was later confirmed by multiple authors [20–22]. Finally, there is some debate about the ordering of the zone-centered phonons, namely, the Raman-active A_g mode and the infrared-active B_u TO mode [22–25].

One crucial material property for high-power electronics is the breakdown field, i.e., the magnitude of the external electric field that a material can sustain before incurring permanent damage. The breakdown field can be computed from first principles using the von Hippel low-energy criterion [26–28] and was recently computed *ab initio* by Mengle and Kioupakis [22] to be 5.4 MV/cm in β-Ga_2O_3 considering only the dominant longitudinal optic (LO) phonon mode. They further estimated that considering all modes would increase the theoretical intrinsic breakdown field by 20% to 6.8 MV/cm. Such calculation assumes total impact ionization for all electrons with energies above the band gap and should therefore be seen as a lower bound; it can also be improved by computing the impact ionization coefficient from first principles [29].

The BFOM [3] describes the current handling capability of a material and is often given relative to silicon. In addition to

*samuel.ponce@epfl.ch
†fgiustino@oden.utexas.edu

the breakdown field, the second material's parameter entering into the BFOM is the intrinsic carrier mobility. The electron room-temperature mobility of β-Ga_2O_3 was computed to be 115 cm^2/Vs at a carrier concentration of 10^{17} cm^{-3}, with a temperature dependence in good agreement with experiment [19], by using Wannier interpolation of the electron-phonon matrix elements [30] and Rode's method [31]. The mobility was also estimated to be below 200 cm^2/Vs using $\mathbf{k}\cdot\mathbf{p}$ perturbation theory [20].

In this context, a careful and detailed analysis of the crystal structure, electronic, optical, vibrational, elastic, and transport properties of β-Ga_2O_3 is warranted. The manuscript is organized as follows. In Sec. II we discuss the relaxed crystal structure of the monoclinic β-Ga_2O_3 and the importance of spin-orbit coupling. Section III is dedicated to the study of the electronic properties, including bandgaps, electronic band structure, and effective masses. In Sec. IV we analyze the phonon dispersion, infrared and Raman spectra, dielectric constant and Born charges, and elastic properties. Section V presents the computed electron and hole carrier mobility with temperature as well as a mode-resolved analysis of the scattering contribution to the mobility. Finally, in Sec. VI we discuss and compute Baliga's figure of merit of β-Ga_2O_3 and compare it with silicon.

II. CRYSTAL STRUCTURE

The crystal structure of β-Ga_2O_3 was originally investigated by Geller to be monoclinic with the C_{2h} $(2/m)$ point group [32] and later refined by Åhman *et al.* [33] using single-crystal diffraction. The measured lattice parameters of the conventional unit cell are $a = 12.214$ Å, $b = 3.037$ Å, $c = 5.798$ Å, and $\beta = 103.83^\circ$ [33]. The conventional cell vectors are $(a, 0, 0)$, $(0, b, 0)$, and $(c\cos\beta, 0, c\sin\beta)$, while the primitive cell vectors are $(\frac{a}{2}, -\frac{b}{2}, 0)$, $(\frac{a}{2}, \frac{b}{2}, 0)$, and $(c\cos\beta, 0, c\sin\beta)$. Any atomic coordinate expressed in the conventional cell (c_x, c_y, c_z) can be expressed in the primitive cell by using the transformation $(c_x - c_y, c_x + c_y, c_z)$. The primitive and conventional cell are made of 10 and 20 atoms, respectively.

The gallium atom sits in two inequivalent positions with octahedral and tetrahedral coordination, respectively. There are three inequivalent oxygen atoms occupying a distorted cubic lattice, with two oxygen atoms being threefold coordinated and one oxygen atom fourfold coordinated. All the five inequivalent atoms have $4i$ Wyckoff position which corresponds to symmetry $(x, 0, z)$ and $(-x, 0, -z)$. The system has four crystal symmetries: the identity, a π rotation around the Cartesian y axis, and their inversions.

To determine the atom positions, we relaxed the lattice parameters and atomic coordinates, starting from the experimental data. We used the QUANTUM ESPRESSO software suite [34] with relativistic local-density approximation (LDA) pseudopotentials from Pseudo Dojo [35], including the $3s^2\ 3p^6\ 3d^{10}\ 4s^2\ 4p^1$ semicore states for gallium and the $2s^2\ 2p^4$ electrons for oxygen. The wave functions were expanded in a plane-wave basis set with energy cutoff of 120 Ry (160 Ry for the elastic response) and a homogeneous Γ-centered Brillouin-zone sampling of $8\times8\times8$ points. We converged the structure such that the maximum force was smaller than 2×10^{-7} Ry/Å and the maximum stress component was lower than 0.07 $Ry/Å^3$. The relaxation yielded the lattice parameters $a = 12.128$ Å, $b = 3.016$ Å, $c = 5.752$ Å, and $\beta = 103.75^\circ$, which slightly underestimates the experimental one as expected from LDA. The relaxed primitive cell crystal structure is shown in Fig. 1 and is formed by two distorted octahedra and two distorted tetrahedra. The gallium and oxygen atoms occupy two and three inequivalent sites at the $4i$ Wyckoff position, respectively, whose coordinates are provided in Table I and are in close agreement with the experimental assignment [33]. The inequivalent gallium-oxygen bond lengths are also reported in Table I, with the tetrahedra having smaller bond lengths than the octahedra. Interestingly, due to their distorted nature, there are two inequivalent Ga_{II}-O_{III} bond lengths in the octahedral configuration, despite having only one inequivalent oxygen position.

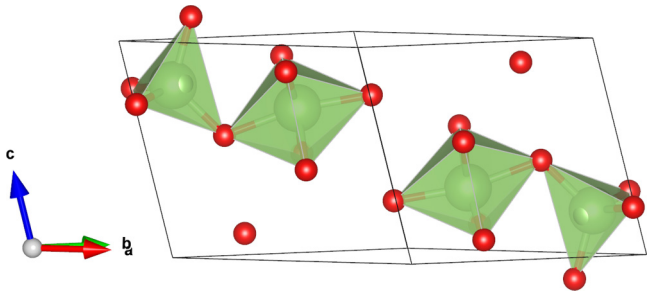

FIG. 1. Relaxed crystal structure of the primitive cell of β-Ga_2O_3 where the large atoms are gallium and the small red atoms are oxygen. Rendered using VESTA [36].

We also report in Table I the volume, density, atomic coordinates, and bond lengths and compare them with experimental data. The calculations were made without spin-orbit coupling (SOC), but we tested that including this effect modifies the crystal data shown in Table I by less than 0.005%. Hence, this effect is neglected for the rest of this work. We finally note that the primitive cell vectors can equivalently be rotated such that $a = b = 11.809$ Å, $c = 10.869$ Å, $\alpha = \beta = 103.335^\circ$, and $\gamma = 27.933^\circ$.

III. ELECTRONIC PROPERTIES

The room-temperature optical band gap of β-Ga_2O_3 obtained through absorption measurements is estimated to be between 4.54 and 4.90 eV [37–39]. Our calculated direct band gap at the zone center is 2.55 eV, strongly underestimating experiments as expected from density functional theory (DFT). In agreement with prior work [15], we find that the valence band maximum (VBM) is located on the $I - L$ high-symmetry lines in the Brillouin zone and yields a slightly smaller indirect band gap of 2.53 eV. A comparison with an earlier work is given in Table II. Our values are consistent with calculations at an equivalent level of theory; hybrid functionals slightly overestimate room-temperature experimental band gaps.

There has been some confusion in the literature about the shape of the Brillouin zone of β-Ga_2O_3 [11,40–43]. The first band structure using the correct monoclinic variation was reported in 2015 [15]. It is therefore important to pay close attention when constructing the Brillouin zone of β-Ga_2O_3.

TABLE I. Experimental and LDA crystal atom coordinates of β-Ga_2O_3 without spin-orbit coupling with conventional unit-cell coordinates (000, $\frac{1}{2}\frac{1}{2}\frac{1}{2}$) $\pm$ ($x0z$) (20 atoms) and primitive cell coordinates $\pm(xxz)$ (10 atoms). In parentheses after the nonequivalent atoms we indicate their Wyckoff position. † There are two inequivalent bond-length Ga_{II}-O_{III} in the octahedral configuration.

Lattice	Experimental [33]	This work
a (Å)	12.214	12.128
b (Å)	3.037	3.016
c (Å)	5.798	5.752
β (°)	103.83	103.750
Volume (Å^3)	104.425	102.190
Density (g/cm^3)	5.961	6.092

	Coordinates			
	Experimental		This work	
Atom	x	z	x	z
Ga_I (4i)	0.09050	0.79460	0.0907608352	0.7951120184
Ga_{II} (4i)	0.34134	0.68598	0.3411450768	0.6855889459
O_I (4i)	0.16450	0.10980	0.1655995553	0.1094726070
O_{II} (4i)	0.49590	0.25660	0.4963406016	0.2557307370
O_{III} (4i)	0.82670	0.43680	0.8269104067	0.4378690351

	Distances (Å)	
Pairs	Experimental [33]	This work
Ga_I-O_I	1.835	1.818
Ga_I-O_{II}	1.833	1.825
Ga_I-O_{III}	1.863	1.852
Ga_{II}-O_I	1.937	1.924
Ga_{II}-O_{II}	1.935	1.919
Ga_{II}-O_{III}	2.005	1.992
Ga_{II}-$O^{\dagger}_{III}$	2.074	2.054

We note that as the definition of two of the primitive cell vectors in the QUANTUM ESPRESSO software are inverted with respect to prior studies, we had to adapt the definition of the high-symmetry points of the Brillouin zone. We give the conversion for clarity in the Table III as well as the value of the four parameters that define the high-symmetry points. To avoid further confusion, the primitive vectors for the base-centered monoclinic Bravais lattice have been modified in QUANTUM ESPRESSO version 6.5 to use the same definition as in the literature [15]. The electronic band structure along high-symmetry lines is given in Fig. 2(a), where the highest valence band and lowest conduction band are highlighted in orange.

We computed the electron effective mass using finite differences, and found 0.267, 0.254, and 0.244 along the Γ-X, Γ-Y, and Γ-Z direction, respectively. The electron effective mass is quite isotropic, with an average value of 0.255 as reported in Table II, which compares well with prior theoretical work and is also close to the experimental value of 0.28 [40,42]. This level of agreement gives us confidence that our calculations of electronic transport properties will be reliable.

In contrast, the hole effective mass at the zone center is highly anisotropic, with very heavy masses along the Γ-X and Γ-Y direction, and a small hole mass of 0.35 m_e along the Γ-Z direction. As a result, this should be an ideal hole transport direction. However, the VBM is not located at the zone centered but 26 meV higher in energy on the I-L line. The transverse and perpendicular hole effective mass at that point is 3.0 m_e and 3.6 m_e, respectively, in agreement with previous

TABLE II. Effective masses of β-Ga_2O_3. The electron effective mass is almost isotropic so we report the average, as done in prior studies. The hole effective mass is reported at Γ as well as at the valence band maximum located between the I and L high-symmetry point. The negative value between the brackets is not an effective mass since the band curvature is positive; this value is reported as a measure of the band curvature.

	Direct gap (eV)	Indirect gap(eV)
This work LDA	2.5532	2.53
LDA [11]	2.188	–
GGA-AM05 [9]	2.377	2.36
HSE+G_0W_0 [9]	5.038	5.05
HSE06 [15]	4.88	4.84
Experiment [37]	–	4.90
Experiment [38]	–	4.54
Experiment [39]	–	4.70

		Hole (m_e)				
	Electron (m_e)	ΓX	ΓY	ΓZ	$IL_\parallel$	$IL_\perp$
This work LDA	0.255	[−78]	3.40	0.35	3.0	3.6
LDA [11]	0.24	–	–	–	2.90	4.19
HSE06 [40]	0.28	–	–	–	–	–
HSE06 [15]	0.275	–	–	–	–	–
B3LYP [41]	0.342	–	–	–	–	–
HSE [9]	0.268	–	–	–	–	–
Experiment [40]	0.28	–	–	–	–	–
Experiment [42]	0.28	–	–	–	–	–

TABLE III. Reciprocal space coordinates of the high-symmetry point in the Brillouin zone of β-Ga_2O_3. $\Psi = \frac{3}{4} - b^2/(4a^2\sin^2\beta)$, $\phi = \Psi - (\frac{3}{4} - \Psi)\frac{a}{c}\cos\beta$, $\zeta = (2 + \frac{a}{c}\cos\beta)/(4\sin^2\beta)$, $\eta = \frac{1}{2} - 2\zeta\frac{c}{a}\cos\beta$.

	Coordinates	
Label	Peelaers [15]	This work
N	$(0, \frac{1}{2}, 0)$	$(-\frac{1}{2}, 0, 0)$
X	$(1-\Psi, 1-\Psi, 0)$	$(\Psi-1, 1-\Psi, 0)$
Γ	(0,0,0)	(0,0,0)
M	$(0, \frac{1}{2}, \frac{1}{2})$	$(-\frac{1}{2}, 0, \frac{1}{2})$
I	$(\phi-1, \phi, \frac{1}{2})$	$(-\phi, \phi-1, \frac{1}{2})$
L	$(-\frac{1}{2}, \frac{1}{2}, \frac{1}{2})$	$(-\frac{1}{2}, -\frac{1}{2}, \frac{1}{2})$
F	$(\zeta-1, 1-\zeta, 1-\eta)$	$(\zeta-1, \zeta-1, 1-\eta)$
Y	$(-\frac{1}{2}, \frac{1}{2}, 0)$	$(-\frac{1}{2}, -\frac{1}{2}, 0)$
Γ	(0,0,0)	(0,0,0)
Z	$(0,0,\frac{1}{2})$	$(0,0,\frac{1}{2})$
Ψ	0.734	0.7336
ϕ	0.742	0.7418
ζ	0.397	0.3971
η	0.590	0.5895

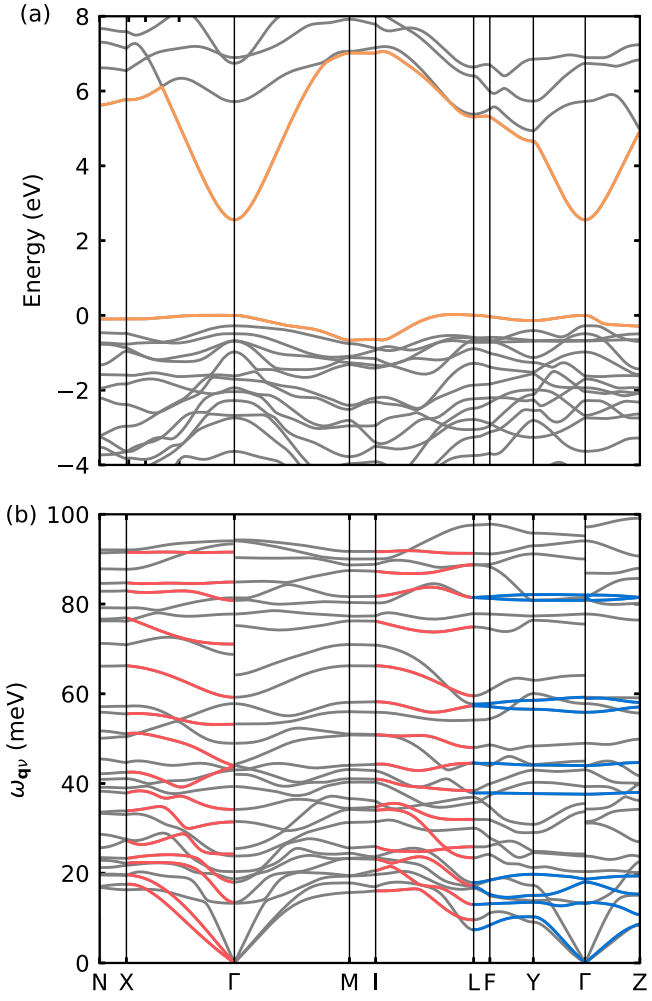

FIG. 2. Electronic (a) and phonon (b) band structure of β-Ga_2O_3 along high-symmetry lines of the monoclinic Brillouin zone. For the phonons, the gray lines denote bands with the identity point group while the red lines have a π rotation around the [0,1,0] Cartesian axis (C_2 point group), and the blue line are lines with inversion symmetry [$C_s(m)$ point group].

work [11]. As transport properties scale inversely with the effective mass, we expect at least an order of magnitude lower hole mobility than the electron mobility.

IV. VIBRATIONAL PROPERTIES

A. Phonon dispersions

We now study the vibrational properties of β-Ga_2O_3 using density functional perturbation theory (DFPT) [45,46]. The calculated phonon band structure along the monoclinic Brillouin zone is presented in Fig. 2(b).

The point groups along high-symmetry lines are either $C_s(m)$ or C_2. The $C_s(m)$ point group contains two symmetry operations: the identity operation E and a mirror plane σ. This point group possess two irreducible representations: the phonon branches belonging to the A' irreducible representation are symmetric with respect to both the identity operation and reflection through the mirror plane, while the branches belonging to the A'' representation are symmetric with respect to the identity but antisymmetric with respect to reflection [colored in Fig. 2(b) in gray and blue, respectively]. The other point group is the C_2 point group, which contains the identity (gray) and a π rotation around the [0,1,0] Cartesian axis [displayed with red lines in Fig. 2(b)]. Note that some directions in the Brillouin zone are less symmetric and only possess the identity (gray). In addition, specific high-symmetry points have higher symmetries: (i) the point group at the N and M points is $C_i(-1)$ with A_g and A_u symmetry operation; (ii) the point group at the X, I points is $C_2(2)$ with identity E and C_2 with π rotation around the [0,1,0] Cartesian axis; (iii) the point group at the Γ, L, Y, Z point is $C_{2h}(2/m)$ with A_g, B_g, A_u, B_u symmetries.

B. Infrared and Raman spectra

The infrared spectrum as well as polarization and temperature-dependent Raman spectra of bulk β-Ga_2O_3 were first measured by Dohy *et al.* [44] in 1982. The measured normal mode frequencies are reported in Table IV along with more recent measurements and previous *ab-initio* values, and are compared to the calculated frequencies from this work. Our calculated phonon band structure slightly underestimates experiments but they are in better agreement than previous calculations. Overall, our calculations agree with previous theoretical work [22,24,47] with a notable difference: in agreement with experiments [23,25] we find that the $A_g(3)$ Raman-active mode has a lower frequency than the B_u(TO1) mode. The highest phonon frequency at the zone center is a LO mode in the Z direction, with a frequency of 97 meV, very close to the experimental value of 100 meV [25]. However, we note that the highest phonon frequency occurs at the Z point with a value of 99.12 meV (not shown in Table IV). Our predicted Raman-active phonon frequencies are 2.5% within the experimental data [23], with the largest difference being attributed to the $A_g(6)$ mode. Our predicted infrared-active LO modes are even closer, with deviation of 1.4% from experimental data [25], while the agreement with LO modes is not as good, with a deviation of 5.4%.

C. Dielectric constant and Born charges

The high-frequency dielectric tensor is fairly isotropic, with $\varepsilon_{xx} = 3.98$, $\varepsilon_{yy} = 4.09$, and $\varepsilon_{zz} = 4.08$, slightly overestimating the experimental value of 3.53–3.6 [48–50] obtained as an isotropic average in thin films. The slight overestimation of the theoretical dielectric tensor is a direct consequence of the underestimation of the band gap by DFT as the electronic part of the dielectric function is inversely proportional to the band gap [51]. We note one experimental work which obtained a direction-dependent dielectric tensor $\varepsilon_{xx} = 3.7$, $\varepsilon_{yy} = 3.2$, and $\varepsilon_{zz} = 3.7$ [25] using generalized spectroscopic ellipsometry within the infrared and far-infrared spectral region. This anisotropy was not observed in another recent experiment reporting $\varepsilon_{xx} = 3.6$, $\varepsilon_{yy} = 3.58$, and $\varepsilon_{zz} = 3.54$ [52], also using generalized spectroscopic ellipsometry. Our calculations appear to support an isotropic dielectric tensor. β-Ga_2O_3 also possesses one nonzero off-diagonal component of the dielectric tensor, but the computed value was lower than 10^{-4} and therefore is not reported.

TABLE IV. Phonon frequencies (meV) of β-Ga_2O_3 at the zone center using a $16 \times 16 \times 12$ **k**-grid. The three zero-frequency acoustic modes are not reported. The infrared experimental values from Dohy *et al.* [44] are measured by transmission, and the frequency of the maxima lies between the LO and TO frequencies.

		Calculated										Experiment				
Mode		This work				Mengle [22]				Liu [24]		Schubert [25]		Machon [23]	Dohy [44]	
symmetry	Activity		LO_X	LO_Y	LO_Z		LO_{b_1}	LO_{b_2}	LO_{b_3}		LO		LO			Optical
A_g (1)	Raman	13.3007				12.9204				12.9812		–		13.6631	13.7623	
B_g (1)	Raman	13.5463				13.0320				13.8986		–		14.0846	14.1342	
B_g (2)	Raman	18.0406				17.9566				17.5190		–		17.9405	18.2257	
A_u (TO1)	Infrared	18.7039	18.7967	18.7130	18.7071	18.0558	18.0583	18.1005	18.0558	17.5562	18.1637	19.1928	19.3787	–		19.21
A_g (2)	Raman	20.3690				19.8635				20.2590		–		20.9781	20.9533	
A_g (3)	Raman	23.8311				23.1107				25.0820		–		24.8464	24.6729	
B_u (TO1)	Infrared	24.2779	24.2785	24.2801	31.1559	21.7617	22.0556	21.7617	28.5300	23.2470	23.6190	26.5078	33.3518	–		31.00
B_u (TO2)	Infrared	31.4358	31.432	33.6936	31.5417	30.2249	32.8459	30.2249	31.1845	31.1944	32.7938	32.5211	35.4595	–	–	
B_u (TO3)	Infrared	34.2134	34.2175	35.5251	34.2964	33.6679	34.3957	33.6679	33.6853	32.8930	35.1619	34.6164	37.8152	–		35.95
A_u (TO2)	Infrared	37.6083	42.9389	37.6085	37.6087	37.5883	38.0446	42.5353	37.5883	36.7241	40.3569	36.7737	42.8861	–		38.43
A_g (4)	Raman	39.3235				38.5678				39.1542		–		39.5014	39.4270	
A_g (5)	Raman	43.0353				42.6692				42.1174		–		42.9481	42.8985	
B_u (TO4)	Infrared	43.7333	43.6516	44.0052	43.9195	43.0151	44.4806	43.0163	43.7515	42.6010	43.9028	44.2376	48.2299	–		46.49
B_g (3)	Raman	44.0051				43.4540				43.1837		–		–	43.7664	
A_g (6)	Raman	48.9601				46.6404				52.0982		–		51.5402	51.4534	
B_u (TO5)	Infrared	53.1958	53.1945	64.0910	58.9781	52.4627	55.2015	52.4627	55.5028	47.5479	63.3063	53.6356	69.6791	–		56.41
A_u (TO3)	Infrared	55.8780	68.7760	55.8787	55.8788	55.5648	60.3258	67.7896	55.5648	50.8955	60.0951	55.6317	73.7706	–		65.09
A_g (7)	Raman	57.8013				56.5566				56.9583		–		–	58.8925	
B_g (4)	Raman	59.2209				58.6049				58.6197		–		58.7065	58.8925	
B_u (TO6)	Infrared	71.0646	71.0662	75.5392	80.8032	70.3586	76.4561	70.3586	82.6541	71.2041	77.5273	70.9810	87.9048	–		79.35
A_g (8)	Raman	77.7683				76.8739				75.2708		–		77.9489	77.8621	
B_g (5)	Raman	80.8029				79.8161				77.7505		–		80.8997	80.7137	
A_g (9)	Raman	81.387				79.9487				81.3460		–		–	81.4576	
A_u (TO4)	Infrared	82.0108	93.3977	82.0111	82.0107	80.9332	81.2282	91.9864	80.9332	80.3294	91.5623	82.2263	95.4678	–		82.82
B_u (TO7)	Infrared	84.8999	84.8976	90.0416	86.8960	83.8146	89.3579	83.8146	85.1660	83.3918	90.2853	85.8467	96.8689	–		89.27
B_u (TO8)	Infrared	91.5781	91.5770	95.1837	97.1831	89.9654	92.5902	89.9654	94.7562	91.9467	94.7983	92.1823	100.4272	–		94.23
A_g (10)	Raman	94.0737				92.3918				93.9428		–		94.7115	94.5999	

The computed diagonal Born effective charges are Ga_I = (2.74, 2.88, 3.04), Ga_{II} = (3.23, 3.42, 3.12), O_I = –(1.46, 2.09, 2.47), O_{II} =–(2.27, 2.25, 1.39), O_{III} =–(2.22, 1.96, 2.28) in units of electron charge. The off-diagonal components are lower than 0.3 and not reported.

D. Elastic properties

The stiffness C_{ij} and compliance $S_{ij} = C_{ij}^{-1}$ tensors link the stress tensor to the strain tensor following the generalized Hooke's law:

$$\sigma_{ij} = C_{ijkl}\varepsilon_{kl}, \tag{1}$$

$$\varepsilon_{ij} = S_{ijkl}\sigma_{kl}, \tag{2}$$

where Einstein's notation is implied.

The Young's modulus E is the linear response of a material to a uniaxial stress where the response is measured in the direction of the applied stress and the bulk modulus B is the response to an isotropic stress. The Young's and bulk moduli can therefore be expressed as a function of a single unit vector in Cartesian space expressed in spherical coordinates $0 \leqslant \theta \leqslant \pi$ and $0 \leqslant \phi \leqslant 2\pi$ as $\mathbf{u} = (\sin\theta\cos\phi, \sin\theta\sin\phi, \cos\theta)$ [60]:

$$E(\theta,\phi) = \frac{1}{u_i u_j u_k u_l S_{ijkl}}, \tag{3}$$

$$B(\theta,\phi) = \frac{1}{u_i u_j S_{ijkk}}, \tag{4}$$

where in the case of the Young modulus we have transformed the head of the compliance tensor from the Cartesian basis to a new basis whose first unit vector is $\mathbf{u}$ following the transformation

$$S'_{1111} = a_{1i}a_{1j}a_{1k}a_{1l}S_{ijkl} = u_i u_j u_k u_l S_{ijkl}, \tag{5}$$

where a_{ij} indicates the direction cosine, specifying the angle between the ith axis of the new basis and the jth axis of the initial basis. The bulk modulus is simpler because it is obtained by applying an isotropic stress (pressure p) such that $\varepsilon_{ij} = -pS_{ijkk}$.

Other elastic properties such as the shear modulus G or Poisson's ratio ν depend on the direction in which the stress is applied $\mathbf{u}$ but also the orthogonal direction in which the response is measured $\mathbf{v}$ and can be parametrized with three angles θ, ϕ, and $0 \leqslant \xi \leqslant 2\pi$:

$$\mathbf{v} = \begin{bmatrix} \cos\theta\cos\phi\cos\xi - \sin\phi\sin\xi \\ \cos\theta\sin\phi\cos\xi + \cos\phi\sin\xi \\ -\sin\theta\cos\xi \end{bmatrix}. \tag{6}$$

The shear modulus and Poisson's ratio can therefore be obtained as

$$G(\theta,\phi,\xi) = \frac{1}{4u_i v_j u_k v_l S_{ijkl}}, \tag{7}$$

$$\nu(\theta,\phi,\xi) = -\frac{u_i u_j v_k v_l S_{ijkl}}{u_i u_j u_k u_l S_{ijkl}}. \tag{8}$$

We note that for the elastic properties studied here we only need up to two vectors (or three angles) in the new basis because the directions of applied stress and measured response are orthogonal, but a general elastic property where this was not the case would require three vectors (or four angles) in the transformed basis.

These elastic properties can be averaged by direct integration on the unit sphere to give the standard Young modulus, bulk modulus, shear modulus, and Poisson's ratio. However, very popular averaging approximations have been developed, including the Voigt approximation, where the average bulk and shear moduli are given by [61]

$$9B_V = C_{11} + C_{22} + C_{33} + 2(C_{12} + C_{13} + C_{23}), \tag{9}$$

$$15G_V = C_{11} + C_{22} + C_{33} - (C_{12} + C_{13} + C_{23}) + 3(C_{44} + C_{55} + C_{66}). \tag{10}$$

In the Reuss approximation, the bulk and shear modulus are defined as [61]

$$B_R^{-1} = S_{11} + S_{22} + S_{33} + 2(S_{12} + S_{13} + S_{23}), \tag{11}$$

$$15G_R^{-1} = 4(S_{11} + S_{22} + S_{33}) - 4(S_{12} + S_{13} + S_{23}) + 3(S_{44} + S_{55} + S_{66}). \tag{12}$$

The Voigt approximation provides an upper bound for the bulk and shear moduli, while the Reuss approximation gives a lower bound. We can therefore define the arithmetic mean, referred to as the Void-Reuss-Hill approximation [61], as $B_H = (B_V + B_R)/2$ and $G_H = (G_V + G_R)/2$. We then express the effective Young E modulus and Poisson ratio ν as

$$E = 9BG/(3B + G), \tag{13}$$

$$\nu = (3B - 2G)/(6B + 2G), \tag{14}$$

where the relations apply to the Voigt, Reuss, and Hill approximation of the Young, bulk, and shear moduli and the Poisson's ratio. We can also define the universal elastic anisotropy as [55]

$$A^U = 5(G_V/G_R) + (B_V/B_R) - 6. \tag{15}$$

Finally, we can obtain the bulk sound velocity v_B, the compressional velocity v_P, shear velocity v_G, and the average sound velocity v_{av} as

$$v_B = \sqrt{B/\rho}, \tag{16}$$

$$v_P = \sqrt{\left(B + \frac{4}{3}G\right)\frac{1}{\rho}}, \tag{17}$$

$$v_G = \sqrt{G/\rho}, \tag{18}$$

$$v_{av} = \left[\frac{1}{3}\left(\frac{2}{v_G^3} + \frac{1}{v_P^3}\right)\right]^{-\frac{1}{3}}, \tag{19}$$

where ρ is the average mass density. Using the average sound velocity, the Debye temperature can be estimated within the Debye model as

$$\Theta_D = \frac{h}{k_B}v_{av}\left[\frac{3N_{at}}{4\pi\rho}\right]^{1/3}, \tag{20}$$

where h, k_B, and N_{at} are the Planck constant, Boltzmann constant, and the number of atoms in the primitive cell, respectively.

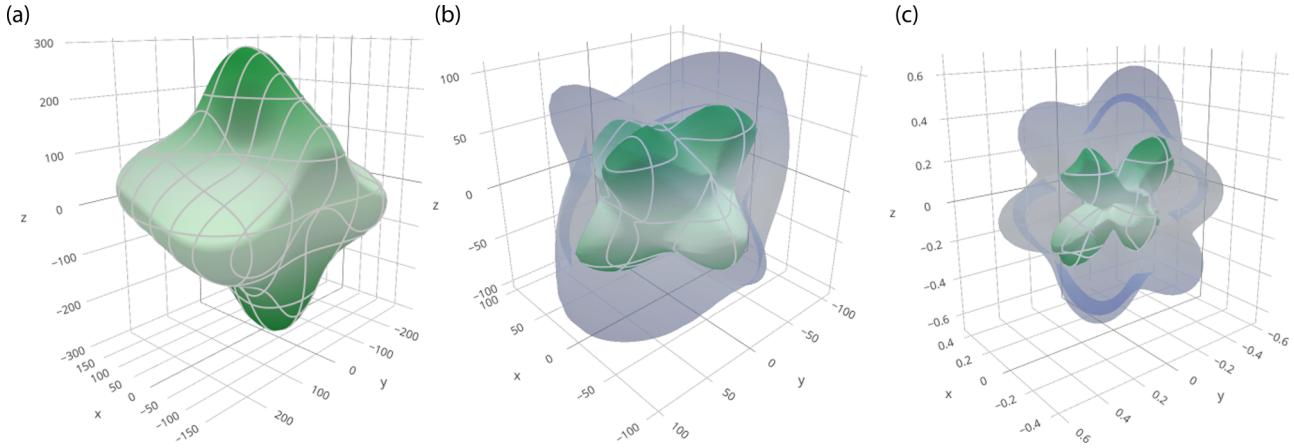

FIG. 3. Spatial dependence of the (a) Young modulus, (b) shear modulus, and (c) Poisson's ratio of β-Ga_2O_3 using the ELATE software [59] for visualization of second-order elastic constants. In (b), (c) the blue and green surfaces represent the maximum and minimum of the third-angle parametrization, see text. The directions x, y, and z represent the increments along the a, b, and c directions of the primitive cell shown in Fig. 1.

We studied the elastic properties of β-Ga_2O_3 using the THERMO_PW code [62]. The stiffness tensor of Laue class C_{2h} for base centered monoclinic crystals has 13 independent elastic constants written in Voigt notation as follows: C_{11}, C_{12}, C_{13}, C_{15}, C_{22}, C_{23}, C_{25}, C_{33}, C_{35}, C_{44}, C_{46}, C_{55}, and C_{66}. The stiffness matrix C_{ij} was obtained by third-order polynomial fitting using 12 deformations with strain intervals of 0.001 to remain in the linear regime. The strains were applied along the crystal lattice vector of the β-Ga_2O_3 primitive cell presented in Fig. 1 such that the resulting stiffness matrix is expressed in that basis. For each strain, the ions were relaxed to their equilibrium positions with a very tight convergence threshold of 4×10^{-6} Ry/Å on forces. We used a 160-Ry energy cutoff on plane waves and a $12 \times 12 \times 9$ **k**-point grid. All the elastic coefficients and elastic properties are reported in Table V. Our calculations compare well with prior theoretical work and with resonant ultrasound spectroscopy coupled with laser-Doppler interferometry [53]. We computed all coefficients independently such that we can estimate off-diagonal accuracy when symmetry constraints are not precisely fulfilled. The most sensitive coefficient is the C_{12}, with an accuracy of ±3.4 GPa.

Using Eqs. (9)–(14), we obtained a bulk modulus of 184 GPa, a Young modulus of 207 GPa, a shear modulus of 79 GPa, and a Poisson's ratio of 0.313. Those numbers agree well with recent experimental elastic constants of $B =$ 183 GPa, $E = 210$ GPa, $G = 80$ GPa, and $\nu = 0.31$ [53]. Finally, using Eqs. (15), (17)–(19), and (20), we compute the universal elastic anisotropy A^{U} to be 0.84, the average sound velocity to be 4.01 km/s, and the estimated Debye temperature Θ_{D} to be 551 K.

Using the ELATE software [59,60], we show in Fig. 3(a) the parametrized Young modulus of Eq. (3) as a parametrized three-dimensional surface and in Figs. 3(b) and 3(c) the parametrized shear modulus and Poisson's ratio of Eqs. (7) and (8), where the maximum and minimum value of the third angle is shown in blue and green, respectively. Compared to simple semiconductors where the bulk modulus is spherical, β-Ga_2O_3 is strongly anisotropic. For example, the Young modulus has a minimum value of 134 GPa in the xz plane with a unit vector (0.94, 0, 0.34), while the maximum value of the Young modulus is 293 GPa in the (0.34, 0.93, 0.13) direction. In the case of the shear modulus and the Poisson's ratio presented in Fig. 3, they are also highly anisotropic, with values ranging from 50 to 133 GPa for the shear modulus and from 0 to 0.67 for the Poisson's ratio, which displays a flowerlike shape along the diagonal axes.

V. CARRIER MOBILITY

We now analyze the intrinsic carrier transport properties of β-Ga_2O_3. We compute the *ab initio* drift carrier mobility

$$\mu_{\alpha\beta} = \frac{e}{V_{\mathrm{uc}} n_{\mathrm{c}}} \sum_n \int \frac{d^3k}{\Omega_{\mathrm{BZ}}} v^{\alpha}_{n\mathbf{k}} \partial_{E_\beta} f_{n\mathbf{k}} \tag{21}$$

through the linear response $\partial_{E_\beta} f_{n\mathbf{k}}$ of the electronic occupation function $f_{n\mathbf{k}}$ to the electric field $\mathbf{E}$, where V_{uc} is the unit-cell volume, Ω_{BZ} the first Brillouin-zone volume, and $n_{\mathrm{c}} = (1/V_{\mathrm{uc}}) \sum_n \int (d^3k/\Omega_{\mathrm{BZ}}) f_{n\mathbf{k}}$ is the carrier concentration. We solve the linearized Boltzmann transport equation (BTE) [63,64],

$$\begin{aligned}\partial_{E_\beta} f_{n\mathbf{k}} = e v^{\beta}_{n\mathbf{k}} \frac{\partial f_{n\mathbf{k}}}{\partial \varepsilon_{n\mathbf{k}}} \tau_{n\mathbf{k}} + \frac{2\pi \tau_{n\mathbf{k}}}{\hbar} \sum_{m\nu} \int \frac{d^3q}{\Omega_{\mathrm{BZ}}} |g_{mn\nu}(\mathbf{k}, \mathbf{q})|^2 \\ \times [(n_{\mathbf{q}\nu} + 1 - f_{n\mathbf{k}}) \delta(\varepsilon_{n\mathbf{k}} - \varepsilon_{m\mathbf{k}+\mathbf{q}} + \hbar\omega_{\mathbf{q}\nu}) \\ + (n_{\mathbf{q}\nu} + f_{n\mathbf{k}}) \delta(\varepsilon_{n\mathbf{k}} - \varepsilon_{m\mathbf{k}+\mathbf{q}} - \hbar\omega_{\mathbf{q}\nu})] \partial_{E_\beta} f_{m\mathbf{k}+\mathbf{q}},\end{aligned} \tag{22}$$

with $\tau_{n\mathbf{k}}$ being the total scattering lifetime,

$$\begin{aligned}\tau^{-1}_{n\mathbf{k}} = \frac{2\pi}{\hbar} \sum_{m\nu} \int \frac{d\mathbf{q}}{\Omega_{\mathrm{BZ}}} |g_{mn\nu}(\mathbf{k}, \mathbf{q})|^2 \\ \times [(n_{\mathbf{q}\nu} + 1 - f_{m\mathbf{k}+\mathbf{q}}) \delta(\varepsilon_{n\mathbf{k}} - \varepsilon_{m\mathbf{k}+\mathbf{q}} - \hbar\omega_{\mathbf{q}\nu}) \\ + (n_{\mathbf{q}\nu} + f_{m\mathbf{k}+\mathbf{q}}) \delta(\varepsilon_{n\mathbf{k}} - \varepsilon_{m\mathbf{k}+\mathbf{q}} + \hbar\omega_{\mathbf{q}\nu})].\end{aligned} \tag{23}$$

Here $v_{n\mathbf{k}}$ is the electronic velocity of the eigenstates $\varepsilon_{n\mathbf{k}}$, $f_{n\mathbf{k}}$ is the Fermi-Dirac occupation, and $n_{\mathbf{q}\nu}$ is the Bose-Einstein distribution function. The electron-phonon matrix elements $g_{mn\nu}(\mathbf{k}, \mathbf{q})$ are the probability amplitude for scattering from

TABLE V. Comparison between our calculated elastic constants C_{ij}, bulk modulus B_H, Young modulus E_H, shear modulus G_H, Poisson's ratio ν_H, universal elastic anisotropy A^U, bulk sound velocity v_B, compressional velocity v_P, shear velocity v_G, average velocity v_{av}, and Debye temperature Θ_D, and prior theoretical and experimental work. The subscript H denotes the Void-Reuss-Hill averaging approximation.

This work	C_{11} GPa	C_{12} GPa	C_{13} GPa	C_{15} GPa	C_{22} GPa	C_{23} GPa	C_{25} GPa	C_{33} GPa
LDA	242	127 ±3.4	140 ±0.0	–17.7 ±0.3	360	90.3 ±0.7	12.0 ±0.4	355
Previous								
LDA [53]	219	127	169	–1.4	365	106	3.5	344
AM05 [9]	223	116	125	–17	333	75	12	330
GGA [54,55]	199	112	125	–2	312	62	1	298
PBESOL [56]	227	128	135	–3.6	335	73	0	313
PBESOL [57]	208	118	146	0	335	83	0	318
Exp. [58]	238	130	152	–4	359	78	2	346
Exp. [53]	243	128	160	–1.6	344	71	0.4	347

This work	C_{35} GPa	C_{44} GPa	C_{46} GPa	C_{55} GPa	C_{66} GPa	B_H GPa	E_H GPa	G_H GPa
LDA	7.7 ±0.5	58	19.7 ±0.3	69	97	184	207	79
Previous								
LDA [53]	18	54	13	76	99	189	198	74
AM05 [9]	7	50	17	69	94	167	194	74
GGA [54,55]	17	39	3	77	95	155	182	70
PBESOL [56]	18	45	6.4	83	99	177	207	79
PBESOL [57]	19	50	9	77	96	171	192	73
Exp. [58]	19	49	6	91	107	184	213	82
Exp. [53]	1	48	5.6	89	104	183	210	80

This work	ν_H	A^U	v_B km/s	v_P km/s	v_G km/s	v_{av} km/s	Θ_D K
LDA	0.31	0.84	5.48	6.87	3.59	4.01	551
Previous							
LDA [53]	0.33	0.93	5.55	6.86	3.49	3.91	538
AM05 [9]	0.31	0.92	5.23	6.60	3.49	3.90	536
GGA [54,55]	0.31	1.04	5.04	6.37	3.37	3.77	518
PBESOL [56]	0.31	0.70	5.38	6.80	3.60	4.03	553
PBESOL [57]	0.31	0.85	5.28	6.62	3.46	3.87	532
Exp. [58]	0.31	0.90	5.48	6.91	3.65	4.08	561
Exp. [53]	0.31	0.88	5.47	6.88	3.62	4.04	556

an initial state $n\mathbf{k}$ to a final state $m\mathbf{k}+\mathbf{q}$ via the emission or absorption of a phonon of frequency $\omega_{\mathbf{q}\nu}$. A common approximation, known as the self-energy relaxation time approximation (SERTA), consists in neglecting the second term on the right-hand side of Eq. (22). The mobility then takes the simpler form:

$$\mu_{\alpha\beta}^{\mathrm{SERTA}} = \frac{1}{V_{\mathrm{uc}} n_c} \sum_n \int \frac{d^3k}{\Omega_{\mathrm{BZ}}} v_{n\mathbf{k}}^{\alpha} v_{n\mathbf{k}}^{\beta} \tau_{n\mathbf{k}}. \tag{24}$$

We used the EPW software [30,65] to interpolate the electron-phonon matrix element $g_{mn\nu}(\mathbf{k},\mathbf{q})$ from a coarse $8\times8\times6$ $\mathbf{k}$-point and $4\times4\times3$ $\mathbf{q}$-point grid to dense $160\times160\times120$ $\mathbf{k}$ and $\mathbf{q}$ grids, as required to converge the electron mobility. The interpolation uses the maximally localized Wannier function [66] and the WANNIER90 software [67]. We used 22 Wannier functions of initial s character centered on the gallium atoms and of p character centered on the oxygen atoms. The Dirac δ functions in Eqs. (22) and (23) were computed using the adaptive smearing method of Refs. [68,69].

To reduce computational costs, we computed separately the electron and hole mobility by explicitly interpolating only the matrix elements for which their electronic eigenvalues at $\mathbf{k}$ and $\mathbf{k}+\mathbf{q}$ were within 0.3 eV of the band edges. We also relied on crystal symmetries to decrease the number of $\mathbf{k}$ points. In the case of the electron mobility, we explicitly interpolated 13 516 $\mathbf{k}$ points and 101 346 $\mathbf{q}$ points, instead of the 3 072 000 points that would have been required by computing all the points from the $160\times160\times120$ grid. In the case of the hole mobility, owing to very flat bands the majority of grid points contribute to the hole mobility, as can be seen in Fig. 2(a). Thus the computational cost is much higher and our densest interpolated grid is $56\times56\times42$ points, which corresponds to 55 892 $\mathbf{k}$ points and 131 712 $\mathbf{q}$ points explicitly computed.

We obtained the following room-temperature electron and hole drift mobility tensor ($\mathrm{cm}^2/\mathrm{Vs}$) in the SERTA:

$$\mu_{\alpha\beta,e}^{\mathrm{SERTA}} = \begin{bmatrix} 170 & 0 & 2.6 \\ 0 & 165 & 0 \\ 2.6 & 0 & 166 \end{bmatrix},$$

$$\mu_{\alpha\beta,h}^{\mathrm{SERTA}} = \begin{bmatrix} 1.1 & 0 & -0.3 \\ 0 & 0.6 & 0 \\ -0.3 & 0 & 1.6 \end{bmatrix}. \tag{25}$$

The results using the self-consistent BTE are

$$\mu_{\alpha\beta,e}^{\mathrm{BTE}} = \begin{bmatrix} 258 & 0 & 7.5 \\ 0 & 277 & 0 \\ 7.5 & 0 & 239 \end{bmatrix},$$

$$\mu_{\alpha\beta,h}^{\mathrm{BTE}} = \begin{bmatrix} 1.2 & 0 & -0.2 \\ 0 & 0.8 & 0 \\ -0.2 & 0 & 1.7 \end{bmatrix}. \tag{26}$$

Interestingly, although the electron effective mass is isotropic (see Table II), we observe about 15% anisotropy for the electron mobility resulting from anisotropic electron-phonon scattering. This result is in line with the recently observed 10%–15% anisotropy in the electron mobility of β-Ga_2O_3 [16]. Based on our convergence study, with increasing fine grid size we estimate an accuracy of ±3 $\mathrm{cm}^2/\mathrm{Vs}$ for the electron mobility and ±0.5 $\mathrm{cm}^2/\mathrm{Vs}$ for the hole mobility. The anisotropy of the hole mobility is within the uncertainty of the calculations.

The temperature dependence of the BTE electron and hole mobility as a function of temperature is presented in Fig. 4, slightly overestimating experimental data. The isotropic averages of the electron and hole mobility are 258 and 1.2 $\mathrm{cm}^2/\mathrm{Vs}$, respectively. To our knowledge, this may be the first time that the hole mobility of β-Ga_2O_3 is computed from first principles.

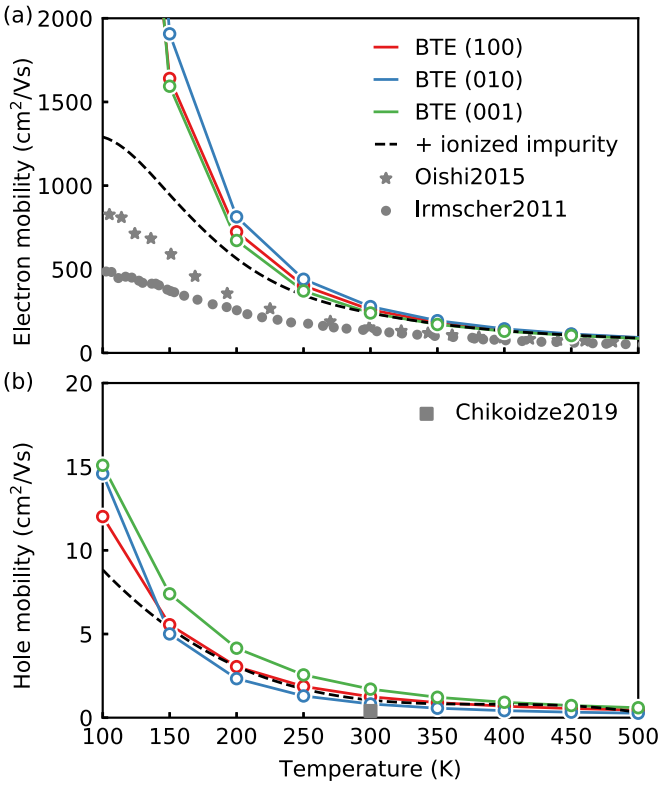

FIG. 4. (a) Electron and (b) hole drift mobility of β-Ga_2O_3 using the Boltzmann transport equation along the three principal directions where the dashed line indicates the direction-averaged drift mobility, including the effect of 10^{15} cm^{-3} ionized impurity scattering. The experimental data of Oishi *et al.* [70], Irmscher *et al.* [12], and Chikoidze *et al.* [71] are Hall measurements of the mobility.

Our room-temperature value of the electron mobility of β-Ga_2O_3 is slightly higher than prior theoretical studies: Ref. [19] gives 115 cm^2/Vs at a carrier concentration of 10^{17} cm^{-3} using Rode's method [31] and 200 cm^2/Vs using $\mathbf{k}\cdot\mathbf{p}$ perturbation theory [20]. Reference [21] obtained an electron mobility of 155 cm^2/Vs using the SERTA, in close agreement with our SERTA value of 167 cm^2/Vs.

The overestimation with respect to experimental electron mobility can be traced back to the fact that our calculated electron effective mass is 7% smaller than in experiments and that the electron-phonon matrix elements are dominated by Fröhlich polar scattering, which in turn scales with the dielectric constant. Our calculated dielectric constant is approximately 11% higher than in experiments. Taken together, these estimates indicate that our calculation underestimates the Fröhlich coupling by approximately 13%. In Ref. [72] we have shown that the mobility is inversely proportional to the Fröhlich coupling and effective mass; therefore we expect that the use of DFT leads to an overestimation of the mobility by approximately 24%. Experimental Hall electron mobilities of 125 cm^2/Vs [12] and 152 cm^2/Vs [70] were reported and are consistent with our findings.

Since lattice scattering becomes negligible at low temperature, the mobility computed using Eq. (21) diverges when T tends to zero. At low temperature other scattering mechanisms dominate carrier transport, including defect [73] and impurity scattering [63]. The impurity scattering may be included using the semi-empirical model developed by Brooks and Herring [74–76]. The ionized-impurity limited mobility $\mu_{\rm i}$ can be evaluated analytically assuming spherical energy surfaces, negligible electron-electron interactions, and complete ionization of the impurities:

$$\mu_{\rm i} = \frac{2^{7/2}\epsilon_s^2(k_{\rm B}T)^{3/2}}{\pi^{3/2}e^3\sqrt{m_d^*}\,n_{\rm i}G(b)} \quad \left[\frac{\rm cm^2}{\rm Vs}\right], \tag{27}$$

where $G(b) = \ln(b+1) - b/(b+1)$, $b = 24\pi m_d^*\epsilon_s(k_{\rm B}T)^2/e^2h^2n'$, and $n' = n(2 - n_{\rm h}/n_{\rm i})$. Here $m_d^* = 0.26\,m_0$ and $3.39\,m_0$ is the density-of-state effective mass for the electron and hole, respectively, n and $n_{\rm i}$ are the electron or hole densities and the density of ionized impurities, respectively, $\epsilon_s = 4.05\epsilon_0$ is the average dielectric constant, ϵ_0 is the permittivity of vacuum, and h is Planck's constant. In the above expressions, the concentrations are expressed in cm^{-3}, and the temperature T is in K. The mobility including phonon (μ) and impurity (μ_i) scattering can be computed using the mixed-scattering formula [76] $\mu_l[1 + X^2\{{\rm ci}(X)\cos(X) + \sin(X)[{\rm si}(X) - \frac{\pi}{2}]\}]$, where $X^2 = 6\mu/\mu_i$ and ci(X) and si(X) are the cosine and sine integrals. The resulting combined mobility for a concentration of 10^{15} cm^{-3} of ionized impurity is shown with a dashed line in Fig. 4, improving the agreement with experiment in the low-temperature regime.

Finally, to shed light on the microscopical mechanisms driving the electron mobility in β-Ga_2O_3 we computed the isotropic average of the momentum and mode-resolved contribution to the SERTA mobility as

$$\mu = \sum_{\mathbf{q}\nu} T_{\mathbf{q}\nu}^{-1}, \tag{28}$$

where the mode-resolved inverse mobility $T_{\mathbf{q}\nu}$ is

$$\begin{aligned} T_{\mathbf{q}\nu} = \frac{6\pi}{\hbar}V_{\rm uc}n_{\rm c}\sum_{mn,\alpha}\int d^3k \frac{w_{\mathbf{q}}|g_{mn\nu}(\mathbf{k},\mathbf{q})|^2}{v_{n\mathbf{k}}^\alpha v_{n\mathbf{k}}^\alpha} \\ \times\,[(n_{\mathbf{q}\nu}+1-f_{m\mathbf{k}+\mathbf{q}})\delta(\varepsilon_{n\mathbf{k}}-\varepsilon_{m\mathbf{k}+\mathbf{q}}-\hbar\omega_{\mathbf{q}\nu}) \\ +\,(n_{\mathbf{q}\nu}+f_{m\mathbf{k}+\mathbf{q}})\delta(\varepsilon_{n\mathbf{k}}-\varepsilon_{m\mathbf{k}+\mathbf{q}}+\hbar\omega_{\mathbf{q}\nu})], \end{aligned} \tag{29}$$

where $w_{\mathbf{q}}$ is the weight of the $\mathbf{q}$ point.

We show in Fig. 5 the mode contribution to the inverse mobility as well as the density of state inverse mobility along with the cumulative integral (dashed red line). The mode contribution spans a region close to the zone center, since as discussed above, larger momenta have negligible contribution to the mobility. The spectral decomposition is separated into three defined energy regions: low-energy ($\hbar\omega < 50$ meV), middle-energy (50 meV $\leqslant \hbar\omega < 71$ meV), and high-energy ($\hbar\omega \geqslant 71$ meV) regions. The high-energy phonons alone account for 62% of the inverse mobility at room temperature, followed by the low-energy phonons (22%) and middle-energy phonons (16%). We mention the following ten modes, in relation with Table IV, that contribute significantly to reducing the mobility: the B_u (LO$_z$: 1−3,8) and B_u (LO$_y$: 2−3, 5−8) modes. Interestingly, all the dominant modes have B_u symmetry and are longitudinal-optical modes.

As can be seen on the left side of Fig. 5, the spectral decomposition of the mode contribution to the inverse mobility is complex, with many modes contributing to the mobility.

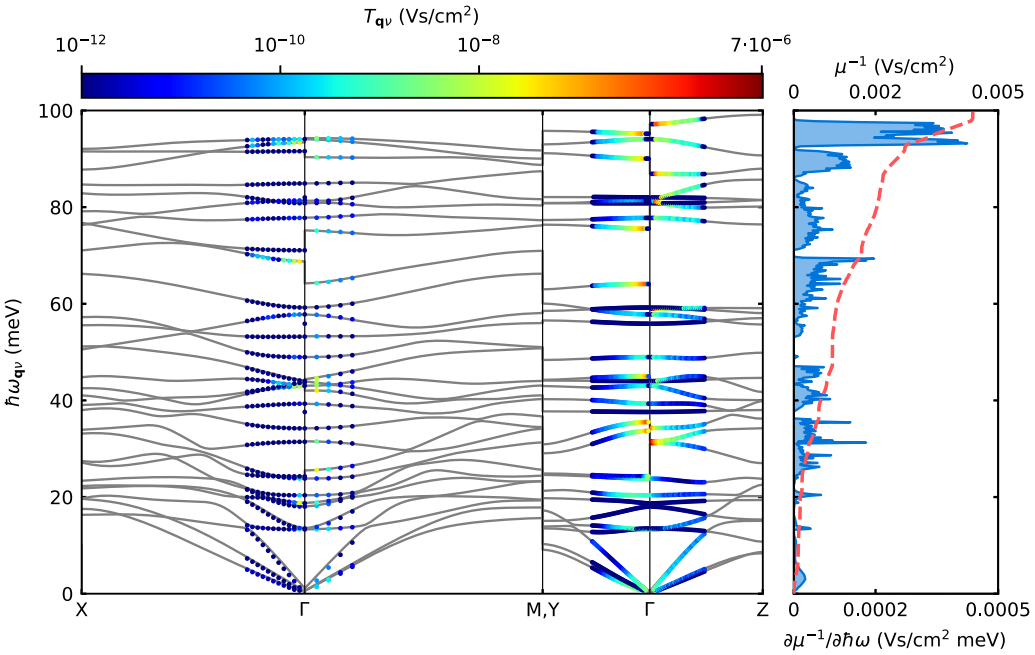

FIG. 5. Direction-averaged momentum and mode-resolved contribution to the inverse electron mobility $T_{\mathbf{q}\nu}$ at room temperature (left) as well as spectral decomposition of the inverse mobility (right). The dashed red line represent the cumulative integral of each spectrum $\partial\mu^{-1}/\partial\hbar\omega$ and adds up to the inverse electron mobility in the self-energy relaxation time approximation.

Such complexity in the phonon spectrum of β-Ga_2O_3 with 30 crossing and intertwined phonon branches translates into many ways for the electrons to interact with the bosonic continuum, yielding increased scattering and reduced mobility. It is worth comparing such behavior of the electron scattering with a related material, wurtzite GaN, that possesses similar electron effective mass $\approx$ 0.2–0.3 m_e. In the nitride compound, the phonon band structure is composed of 12 modes clearly separated by a 20-meV gap [77]. This translates into a reduced scattering with two dominant scatterings at around 2 and 92 meV [78] and explains why the electron mobility in wurtzite GaN is four times larger than in β-Ga_2O_3, despite similar effective masses.

VI. BALIGA'S FIGURE OF MERIT

Figures of merit have been introduced as a way to quantify the influence of materials parameters on the performance of semiconductor devices. The most common figures of merit include the Johnson figure of merit (JFOM), which assesses the quality of a semiconductor for high-frequency power transistor application [79], the Keyes figure of merit (KFOM), which quantifies the thermal limitation of transistor switching frequency [80], and the Baliga figure of merit (BFOM) [3]. In this work we focus solely on the BFOM, which is used to identify materials parameters so as to minimize losses in power field effect transistors [1]. The BFOM relies upon the assumption that power losses are solely due to power dissipation in the on state by current flow through the on resistance of the device. As a result, the BFOM is used for devices operating at low frequency, where the conduction losses are dominant.

The BFOM is given by

$$\text{BFOM} = \epsilon^0 \mu E_b^3, \tag{30}$$

where E_b is the computed breakdown field, μ the computed mobility from Eq. (21), and ϵ^0 is the temperature-dependent experimental static dielectric function with the field perpendicular to the (100), (010), and (001) direction, respectively [81], which we reproduce in Fig. 6(c). Importantly, we stress that all the quantities entering in Eq. (30) are temperature dependent.

The temperature- and direction-dependent mobility has already been obtained in Sec. V. Therefore we only need to compute the breakdown field to obtain the BFOM. References [84,85] proposed the following model:

$$E_b = 24.442 \exp(0.315\sqrt{E_g \omega_{\max}}), \tag{31}$$

where E_g is the band gap of the materials in eV, $\omega_{\max}$ the phonon cutoff frequency in THz, and E_b the breakdown field in MV/m. Although successful, the main limitation of this model is that it is independent of temperature. For this reason, we aim at computing the BFOM from first principles while retaining the temperature dependence. To do so, in addition to the intrinsic carrier mobility, we need to compute the intrinsic breakdown field.

The most common theory for a material breakdown relies on electron avalanche [86], which occurs when the electron energy reaches the threshold for impact ionization. This is the energy at which an electron generates a second conduction electron by excitation across the electronic energy gap, causing electron multiplication (avalanche) and leading to a breakdown of the material [27]. As a result, the threshold for impact ionization is usually taken as the electronic band gap. The idea behind the theory relies on accelerating the conduction

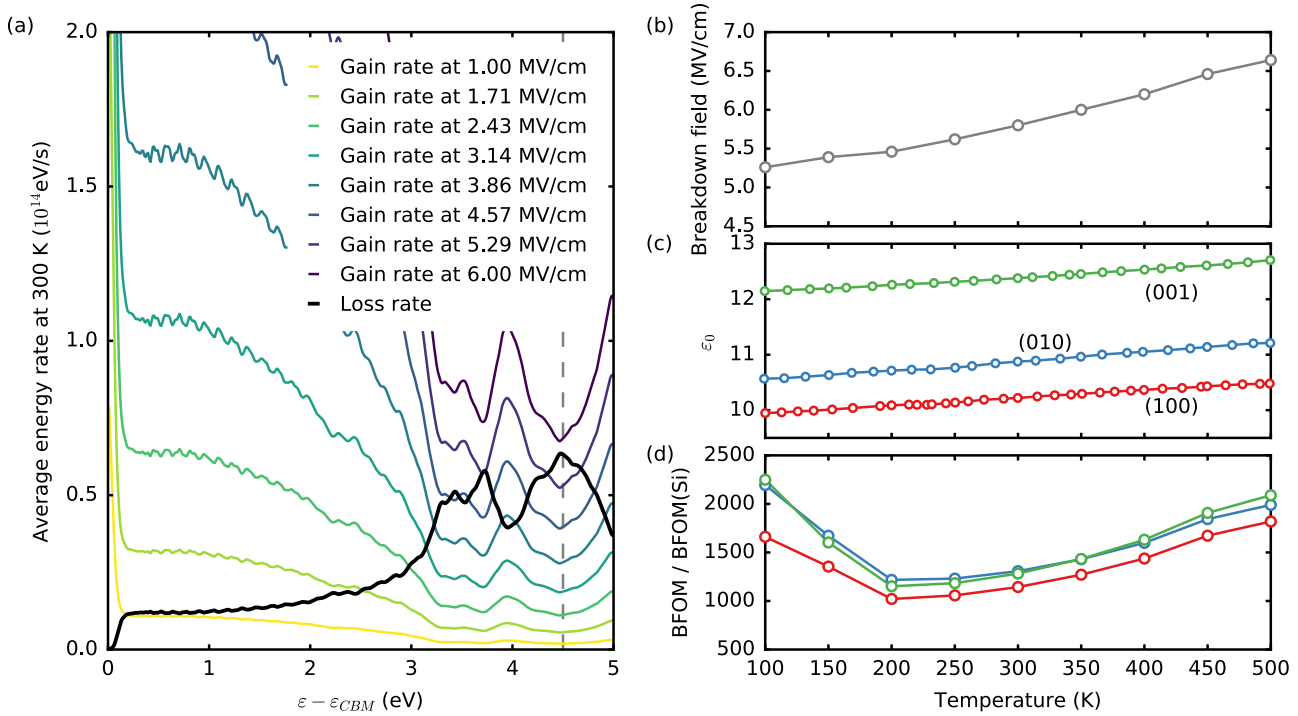

FIG. 6. (a) Average energy-gain rate $A(\varepsilon)$ from an applied external field and average energy loss to the lattice $B(\varepsilon)$. Both quantities are for 300 K. The intrinsic breakdown occurs when the applied electric field is such that the gain rate is larger than the loss rate for all energies between the conduction-band minimum (CBM) and the CBM plus the energy of the band gap (4.5 eV). (b) Variation of computed breakdown field with temperature. (c) Experimental variation of dielectric function with direction and temperature of β-Ga_2O_3 from Ref. [81]. (d) Baliga's figure of merit (BFOM) with respect to the BFOM of silicon. The BFOM of Si was obtained using dielectric constants from Ref. [82] and a breakdown field of 0.3 MV/cm, as well as the experimental electron mobility from Norton *et al.* [83].

electron with a laser field and taking into account the electron scattering with the lattice during pumping. Indeed, the phonon collision reduces the acceleration of the electron by modifying their momentum.

The von Hippel low-energy criterion is more stringent and states that breakdown will occur when the rate of energy gain $A(E, \varepsilon, T)$ by an electron of energy ε due to the external field E at temperature T is larger than the energy-loss rate $B(\varepsilon, T)$ to the lattice due to electron-phonon interaction [26–28]:

$$A(E, \varepsilon, T) > B(\varepsilon, T), \tag{32}$$

for energies ε going from the conduction-band minimum to the threshold for impact ionization, i.e., the band gap of the materials.

The steady-state solution for the average energy-gain rate from the electric field is [27]

$$A(E, \varepsilon, T) = \frac{1}{3}\frac{e^2\tau(\varepsilon, T)}{m^*}E^2, \tag{33}$$

where e^2 is the electron charge and $m^* = 0.3$ [87] the electron effective mass. The energy- and temperature-dependent electron-phonon lifetime is given by

$$\tau^{-1}(\varepsilon, T) = \sum_{n\mathbf{k}} \tau_{n\mathbf{k}}^{-1}(T)\delta(\varepsilon_{n\mathbf{k}} - \varepsilon)/D(\varepsilon), \tag{34}$$

where $D(\varepsilon)$ is the density of state and $\tau_{n\mathbf{k}}^{-1}$ is given by Eq. (23).

The field-independent net rate of energy loss $B(\varepsilon, T)$ to the lattice is obtained by subtracting the rate of phonon absorption from phonon emission [27,28]:

$$B(\varepsilon, T) = \frac{2\pi}{\hbar D(\varepsilon)}\sum_{nm\nu}\iint \frac{d^3k d^3q}{\Omega_{\mathrm{BZ}}^2}|g_{mn\nu}(\mathbf{k}, \mathbf{q})|^2\delta(\varepsilon_{n\mathbf{k}} - \varepsilon) \times \hbar\omega_{\mathbf{q}\nu}[(n_{\mathbf{q}\nu} + 1/2)\delta(\varepsilon_{n\mathbf{k}} - \varepsilon_{m\mathbf{k}+\mathbf{q}} + \hbar\omega_{\mathbf{q}\nu}) - n_{\mathbf{q}\nu}\delta(\varepsilon_{n\mathbf{k}} - \varepsilon_{m\mathbf{k}+\mathbf{q}} - \hbar\omega_{\mathbf{q}\nu})], \tag{35}$$

where $n_{\mathbf{q}\nu}$ are the Bose-Einstein occupation factors in the absence of an electric field.

We computed the energy-gain and energy-loss rates using the EPW software by interpolation on a dense $80 \times 80 \times 60$ **k**-point grid and a $40 \times 40 \times 30$ **q**-point grid with a constant smearing of 20 meV. In Fig. 6(a) we present the change of energy-loss rate as a function of energy, starting from the conduction-band minimum (CBM). On the same figure, we compare the loss rate with the average energy-gain rate for increasing external electric field E at room temperature. We define the intrinsic breakdown field E_b as the smallest external electric field such that the energy-gain curve is larger than the energy-loss curve for all energies between the CBM and the CBM plus the energy of the band gap (4.5 eV). This value provides an estimate of the electric field range for which the material will not undergo dielectric breakdown. We compute that at room temperature the breakdown field is 5.8 MV/cm, including all electron-phonon scattering processes. Using the same approach for different temperatures, we can obtain the change of breakdown field with temperature shown

in Fig. 6(b). We find a breakdown field of 6.64 MV/cm at 500 K.

Such calculation was performed by Mengle and Kioupakis [22] for the intrinsic electron breakdown field at 300 K. They obtained 5.4 MV/cm by considering only the dominant LO phonon mode and estimated that the contribution of other modes would lead to 6.8 MV/cm. We note that the experimental breakdown field in β-Ga_2O_3 is typically reported at around 8 MV/cm [1]. This is in line with our calculations, since the von Hippel low-energy criterion should be seen as a lower bound for the breakdown field.

Using this information and the experimental dielectric function, we can compute the temperature- and direction-dependent BFOM. The BFOM is typically given with respect to the BFOM of silicon.

In this case we computed the reference BFOM of silicon by using the temperature-dependent dielectric constant of Refs. [82,88] and a breakdown field of 0.3 MV/cm, as well as the experimental temperature-dependent electron mobility from Norton *et al.* [83]. The resulting change of BFOM is given in Fig. 6(d). The direction-averaged minimum and maximum values are 1130 and 2035, respectively. We see that even though the computed breakdown field underestimates the experiment, this effect is compensated by an overestimation of the mobility. As a result, our calculated BFOM is close to experimental estimates of 2000–3000 [1]. This cancellation suggests that the current level of theory could be sufficient to predict the BFOM of new materials.

VII. CONCLUSION

In this work, we performed an in-depth study of the structural, vibrational, elastic, electrical, and transport properties of β-Ga_2O_3 using state-of-the-art, first-principles simulation tools. We carefully analyzed the structural properties of the monoclinic variation of β-Ga_2O_3 and analyzed the effect of spin-orbit coupling on those properties. We studied the electronic structure and carrier effective masses. We made a careful analysis of the vibrational properties, including a symmetry analysis of β-Ga_2O_3 using first-order response function theory, including dielectric and Born effective charges study. We calculated many elastic properties by computing the elastic constants tensor, including the bulk, shear, and Young modulus tensor, using parametric three-dimensional visualization but also Poisson's ratio, universal elastic anisotropy, sound velocities, and Debye temperature, and found a strong directional anisotropy. We used the Boltzmann transport equation to compute the intrinsic electron and hole drift mobility and obtained room-temperature values of 258 and 1.2 cm^2/Vs, respectively. We found that the mobility in β-Ga_2O_3 was limited by a series of longitudinal optic phonons with symmetry character B_u at the zone center. Finally, we used the von Hippel low-energy criterion to compute fully from first principles the breakdown field, which allowed us to compute the direction- and temperature-dependent Baliga figure of merit for high-power devices. We saw that the predicted figure of merit was in good agreement with experiment and attributed this to an overestimation of the computed mobility compensating an underestimation in the computed breakdown field.

The present analysis may serve as the basis for a general, consistent, and predictive framework to study materials for power electronics from first principles.

ACKNOWLEDGMENTS

The authors thank Paolo Giannozzi for his help with the monoclinic structure in QUANTUM ESPRESSO and Andrea Dal Corso for his help with the monoclinic structure in the `thermo_pw` code. Computer time was provided by the PRACE-15 and PRACE-17 resources MareNostrum at BSC-CNS, and the Texas Advanced Computing Center (TACC) at the University of Texas at Austin. S.P. acknowledges support from the European Union's Horizon 2020 Research and Innovation Programme under Marie Skłodowska-Curie Grant Agreement SELPH2D No. 839217. F.G.'s contribution to this work was supported as part of the Computational Materials Sciences Program funded by the U.S. Department of Energy, Office of Science, Basic Energy Sciences, under Award No. DE-SC0020129.

[1] Z. Galazka, β-Ga_2O_3 for wide-bandgap electronics and optoelectronics, Semicond. Sci. Technol. **33**, 113001 (2018).

[2] M. Higashiwaki, K. Sasaki, A. Kuramata, T. Masui, and S. Yamakoshi, Gallium oxide (Ga_2O_3) metal-semiconductor field-effect transistors on single-crystal β-Ga_2O_3 (010) substrates, Appl. Phys. Lett. **100**, 013504 (2012).

[3] B. J. Baliga, Semiconductors for high-voltage, vertical channel field-effect transistors, J. Appl. Phys. **53**, 1759 (1982).

[4] M. Higashiwaki and G. H. Jessen, Guest editorial: The dawn of gallium oxide microelectronics, Appl. Phys. Lett. **112**, 060401 (2018).

[5] J. Kong, D. Nordlund, J. S. Jin, S. Y. Kim, S.-M. Jin, D. Huang, Y. Zheng, C. Karpovich, G. Sertic, H. Wang, J. Li, G. Weng, F. Antonio, M. Mariano, S. Maclean, T. Goh, J. Y. Kim, and A. D. Taylor, Underwater organic solar cells via selective removal of electron acceptors near the top electrode, ACS Energy Lett. **4**, 1034 (2019).

[6] E. G. Víllora, K. Shimamura, Y. Yoshikawa, K. Aoki, and N. Ichinose, Large-size β-Ga_2O_3 single crystals and wafers, J. Cryst. Growth **270**, 420 (2004).

[7] H. Aida, K. Nishiguchi, H. Takeda, N. Aota, K. Sunakawa, and Y. Yaguchi, Growth of β-Ga_2O_3 single crystals by the edge-defined, film fed growth method, Jpn. J. Appl. Phys. **47**, 8506 (2008).

[8] K. Nomura, H. Ohta, A. Takagi, T. Kamiya, M. Hirano, and H. Hosono, Room-temperature fabrication of transparent flexible thin-film transistors using amorphous oxide semiconductors, Nature (London) **432**, 488 (2004).

[9] J. Furthmüller and F. Bechstedt, Quasiparticle bands and spectra of Ga_2O_3 polymorphs, Phys. Rev. B **93**, 115204 (2016).

[10] N. Ueda, H. Hosono, R. Waseda, and H. Kawazoe, Anisotropy of electrical and optical properties in β-Ga_2O_3 single crystals, Appl. Phys. Lett. **71**, 933 (1997).

[11] K. Yamaguchi, First principles study on electronic structure of β-Ga_2O_3, Solid State Commun. **131**, 739 (2004).

[12] K. Irmscher, Z. Galazka, M. Pietsch, R. Uecker, and R. Fornari, Electrical properties of β-Ga_2O_3 single crystals grown by the Czochralski method, J. Appl. Phys. **110**, 063720 (2011).

[13] J. B. Varley, J. R. Weber, A. Janotti, and C. G. Van de Walle, Oxygen vacancies and donor impurities in β-Ga_2O_3, Appl. Phys. Lett. **97**, 142106 (2010).

[14] J. B. Varley, H. Peelaers, A. Janotti, and C. G. V. de Walle, Hydrogenated cation vacancies in semiconducting oxides, J. Phys.: Condens. Matter **23**, 334212 (2011).

[15] H. Peelaers and C. G. Van de Walle, Brillouin zone and band structure of β-Ga_2O_3, Phys. Status Solidi B **252**, 828 (2015).

[16] M. H. Wong, K. Sasaki, A. Kuramata, S. Yamakoshi, and M. Higashiwaki, Electron channel mobility in silicon-doped Ga_2O_3 MOSFETs with a resistive buffer layer, Jpn. J. Appl. Phys. **55**, 1202B9 (2016).

[17] K. Ghosh, A. Kumar, and U. Singisetti, *Electrical Properties 2*, Springer Series in Materials Science Vol. 293 (Springer, Cham, 2020).

[18] A. Parisini and R. Fornari, Analysis of the scattering mechanisms controlling electron mobility in β-Ga_2O_3 crystals, Semicond. Sci. Technol. **31**, 035023 (2016).

[19] K. Ghosh and U. Singisetti, Ab initio calculation of electron-phonon coupling in monoclinic β-Ga_2O_3 crystal, Appl. Phys. Lett. **109**, 072102 (2016).

[20] N. Ma, N. Tanen, A. Verma, Z. Guo, T. Luo, H. G. Xing, and D. Jena, Intrinsic electron mobility limits in β-Ga_2O_3, Appl. Phys. Lett. **109**, 212101 (2016).

[21] Y. Kang, K. Krishnaswamy, H. Peelaers, and C. G. V. de Walle, Fundamental limits on the electron mobility of β-Ga_2O_3, J. Phys.: Condens. Matter **29**, 234001 (2017).

[22] K. A. Mengle and E. Kioupakis, Vibrational and electron-phonon coupling properties of β-Ga_2O_3 from first-principles calculations: Impact on the mobility and breakdown field, AIP Adv. **9**, 015313 (2019).

[23] D. Machon, P. F. McMillan, B. Xu, and J. Dong, High-pressure study of the β-to-α transition in Ga_2O_3, Phys. Rev. B **73**, 094125 (2006).

[24] B. Liu, M. Gu, and X. Liu, Lattice dynamical, dielectric, and thermodynamic properties of β-Ga_2O_3 from first principles, Appl. Phys. Lett. **91**, 172102 (2007).

[25] M. Schubert, R. Korlacki, S. Knight, T. Hofmann, S. Schöche, V. Darakchieva, E. Janzén, B. Monemar, D. Gogova, Q.-T. Thieu, R. Togashi, H. Murakami, Y. Kumagai, K. Goto, A. Kuramata, S. Yamakoshi, and M. Higashiwaki, Anisotropy, phonon modes, and free charge carrier parameters in monoclinic β-gallium oxide single crystals, Phys. Rev. B **93**, 125209 (2016).

[26] A. Von Hippel, Electric breakdown of solid and liquid insulators, J. Appl. Phys. **8**, 815 (1937).

[27] M. Sparks, D. L. Mills, R. Warren, T. Holstein, A. A. Maradudin, L. J. Sham, E. Loh, and D. F. King, Theory of electron-avalanche breakdown in solids, Phys. Rev. B **24**, 3519 (1981).

[28] Y. Sun, S. A. Boggs, and R. Ramprasad, The intrinsic electrical breakdown strength of insulators from first principles, Appl. Phys. Lett. **101**, 132906 (2012).

[29] K. Ghosh and U. Singisetti, Impact ionization in β-Ga_2O_3, J. Appl. Phys. **124**, 085707 (2018).

[30] S. Poncé, E. Margine, C. Verdi, and F. Giustino, EPW: Electron-phonon coupling, transport and superconducting properties using maximally localized Wannier functions, Comput. Phys. Commun. **209**, 116 (2016).

[31] D. L. Rode, Low-field electron transport, Semicond. Semimet. **10**, 1 (1975).

[32] S. Geller, Crystal structure of β-Ga_2O_3, J. Chem. Phys. **33**, 676 (1960).

[33] J. Åhman, G. Svensson, and J. Albertsson, A reinvestigation of β-gallium oxide, Acta Crystallogr. Sect. C **52**, 1336 (1996).

[34] P. Giannozzi, O. Andreussi, T. Brumme, O. Bunau, M. B. Nardelli, M. Calandra, R. Car, C. Cavazzoni, D. Ceresoli, M. Cococcioni, N. Colonna, I. Carnimeo, A. D. Corso, S. de Gironcoli, P. Delugas, R. A. DiStasio, A. Ferretti, A. Floris, G. Fratesi, G. Fugallo *et al.*, Advanced capabilities for materials modelling with quantum ESPRESSO, J. Phys.: Condens. Matter **29**, 465901 (2017).

[35] M. van Setten, M. Giantomassi, E. Bousquet, M. Verstraete, D. Hamann, X. Gonze, and G.-M. Rignanese, The pseudodojo: Training and grading a 85 element optimized norm-conserving pseudopotential table, Comput. Phys. Commun. **226**, 39 (2018).

[36] K. Momma and F. Izumi, *VESTA3* for three-dimensional visualization of crystal, volumetric and morphology data, J. Appl. Crystallogr. **44**, 1272 (2011).

[37] M. Orita, H. Ohta, M. Hirano, and H. Hosono, Deep-ultraviolet transparent conductive β-Ga_2O_3 thin films, Appl. Phys. Lett. **77**, 4166 (2000).

[38] T. Matsumoto, M. Aoki, A. Kinoshita, and T. Aono, Absorption and reflection of vapor grown single crystal platelets of β-Ga_2O_3, Jpn. J. Appl. Phys. **13**, 1578 (1974).

[39] H. H. Tippins, Optical absorption and photoconductivity in the band edge of β-Ga_2O_3, Phys. Rev. **140**, A316 (1965).

[40] M. Mohamed, C. Janowitz, I. Unger, R. Manzke, Z. Galazka, R. Uecker, R. Fornari, J. R. Weber, J. B. Varley, and C. G. Van de Walle, The electronic structure of β-Ga_2O_3, Appl. Phys. Lett. **97**, 211903 (2010).

[41] H. He, R. Orlando, M. A. Blanco, R. Pandey, E. Amzallag, I. Baraille, and M. Rérat, First-principles study of the structural, electronic, and optical properties of Ga_2O_3 in its monoclinic and hexagonal phases, Phys. Rev. B **74**, 195123 (2006).

[42] C. Janowitz, V. Scherer, M. Mohamed, A. Krapf, H. Dwelk, R. Manzke, Z. Galazka, R. Uecker, K. Irmscher, R. Fornari, M. Michling, D. Schmeißer, J. R. Weber, J. B. Varley, and C. G. V. de Walle, Experimental electronic structure of In_2O_3 and Ga_2O_3, New J. Phys. **13**, 085014 (2011).

[43] F. Litimein, D. Rached, R. Khenata, and H. Baltache, FPLAPW study of the structural, electronic, and optical properties of Ga_2O_3: Monoclinic and hexagonal phases, J. Alloys Compd. **488**, 148 (2009).

[44] D. Dohy, G. Lucazeau, and A. Revcolevschi, Raman spectra and valence force field of single-crystalline β-Ga_2O_3, J. Solid State Chem. **45**, 180 (1982).

[45] X. Gonze and C. Lee, Dynamical matrices, Born effective charges, dielectric permittivity tensors, and interatomic force

constants from density-functional perturbation theory, Phys. Rev. B **55**, 10355 (1997).

[46] S. Baroni, S. de Gironcoli, A. Dal Corso, and P. Giannozzi, Phonons and related crystal properties from density-functional perturbation theory, Rev. Mod. Phys. **73**, 515 (2001).

[47] M. D. Santia, N. Tandon, and J. D. Albrecht, Lattice thermal conductivity in β-Ga_2O_3 from first principles, Appl. Phys. Lett. **107**, 041907 (2015).

[48] M. Passlack, E. F. Schubert, W. S. Hobson, M. Hong, N. Moriya, S. N. G. Chu, K. Konstadinidis, J. P. Mannaerts, M. L. Schnoes, and G. J. Zydzik, Ga_2O_3 films for electronic and optoelectronic applications, J. Appl. Phys. **77**, 686 (1995).

[49] M. Rebien, W. Henrion, M. Hong, J. P. Mannaerts, and M. Fleischer, Optical properties of gallium oxide thin films, Appl. Phys. Lett. **81**, 250 (2002).

[50] G. Schmitz, P. Gassmann, and R. Franchy, A combined scanning tunneling microscopy and electron energy loss spectroscopy study on the formation of thin, well-ordered β-Ga_2O_3 films on CoGa(001), J. Appl. Phys. **83**, 2533 (1998).

[51] M. Lee, Y. Youn, K. Yim, and S. Han, High-throughput ab initio calculations on dielectric constant and band gap of non-oxide dielectrics, Sci. Rep. **8**, 14794 (2018).

[52] C. Sturm, R. Schmidt-Grund, C. Kranert, J. Furthmüller, F. Bechstedt, and M. Grundmann, Dipole analysis of the dielectric function of color dispersive materials: Application to monoclinic Ga_2O_3, Phys. Rev. B **94**, 035148 (2016).

[53] K. Adachi, H. Ogi, N. Takeuchi, N. Nakamura, H. Watanabe, T. Ito, and Y. Ozaki, Unusual elasticity of monoclinic β-Ga_2O_3, J. Appl. Phys. **124**, 085102 (2018).

[54] A. Jain, S. P. Ong, G. Hautier, W. Chen, W. D. Richards, S. Dacek, S. Cholia, D. Gunter, D. Skinner, G. Ceder, and K. A. Persson, The materials project: A materials genome approach to accelerating materials innovation, APL Mater. **1**, 011002 (2013).

[55] M. de Jong, W. Chen, T. Angsten, A. Jain, R. Notestine, A. Gamst, M. Sluiter, C. K. Ande, S. van der Zwaag, J. J. Plata, C. Toher, S. Curtarolo, G. Ceder, K. A. Persson, and M. Asta, Charting the complete elastic properties of inorganic crystalline compounds, Sci. Data **2**, 150009 (2015).

[56] A. S. Grashchenko, S. A. Kukushkin, V. I. Nikolaev, A. V. Osipov, E. V. Osipova, and I. P. Soshnikov, Study of the anisotropic elastoplastic properties of β-Ga_2O_3 films synthesized on SiC/Si substrates, Phys. Solid State **60**, 852 (2018).

[57] A. V. Osipov, A. S. Grashchenko, S. A. Kukushkin, V. I. Nikolaev, E. V. Osipova, A. I. Pechnikov, and I. P. Soshnikov, Structural and elastoplastic properties of β-Ga_2O_3 films grown on hybrid SiC/Si substrates, Continuum Mech. Thermodyn. **30**, 1059 (2018).

[58] W. Miller, K. Böttcher, Z. Galazka, and J. Schreuer, Numerical modeling of the Zzochralski growth of β-Ga_2O_3, Crystals **7**, 26 (2017).

[59] R. Gaillac, P. Pullumbi, and F.-X. Coudert, ELATE: An open-source online application for analysis and visualization of elastic tensors, J. Phys.: Condens. Matter **28**, 275201 (2016).

[60] A. Marmier, Z. A. Lethbridge, R. I. Walton, C. W. Smith, S. C. Parker, and K. E. Evans, ElAM: A computer program for the analysis and representation of anisotropic elastic properties, Comput. Phys. Commun. **181**, 2102 (2010).

[61] R. Hill, The elastic behaviour of a crystalline aggregate, Proc. Phys. Soc. Sect. A **65**, 349 (1952).

[62] A. D. Corso, Elastic constants of beryllium: A first-principles investigation, J. Phys.: Condens. Matter **28**, 075401 (2016).

[63] S. Poncé, E. R. Margine, and F. Giustino, Towards predictive many-body calculations of phonon-limited carrier mobilities in semiconductors, Phys. Rev. B **97**, 121201(R) (2018).

[64] S. Poncé, W. Li, S. Reichardt, and F. Giustino, First-principles calculations of charge carrier mobility and conductivity in bulk semiconductors and two-dimensional materials, Rep. Prog. Phys. **83**, 036501 (2020).

[65] F. Giustino, M. L. Cohen, and S. G. Louie, Electron-phonon interaction using Wannier functions, Phys. Rev. B **76**, 165108 (2007).

[66] N. Marzari, A. A. Mostofi, J. R. Yates, I. Souza, and D. Vanderbilt, Maximally localized Wannier functions: Theory and applications, Rev. Mod. Phys. **84**, 1419 (2012).

[67] G. Pizzi, V. Vitale, R. Arita, S. Blügel, F. Freimuth, G. Géranton, M. Gibertini, D. Gresch, C. Johnson, T. Koretsune, J. Ibañez-Azpiroz, H. Lee, J.-M. Lihm, D. Marchand, A. Marrazzo, Y. Mokrousov, J. I. Mustafa, Y. Nohara, Y. Nomura, L. Paulatto *et al.*, Wannier90 as a community code: New features and applications, J. Phys.: Condens. Matter **32**, 165902 (2020).

[68] W. Li, J. Carrete, N. A. Katcho, and N. Mingo, ShengBTE: A solver of the Boltzmann transport equation for phonons, Comput. Phys. Commun. **185**, 1747 (2014).

[69] W. Li, Electrical transport limited by electron-phonon coupling from Boltzmann transport equation: An *ab initio* study of Si, Al, and MoS_2, Phys. Rev. B **92**, 075405 (2015).

[70] T. Oishi, Y. Koga, K. Harada, and M. Kasu, High-mobility β-$Ga_2O_3(\bar{2}01)$ single crystals grown by edge-defined film-fed growth method and their Schottky barrier diodes with Ni contact, Appl. Phys. Express **8**, 031101 (2015).

[71] E. Chikoidze, C. Sartel, H. Mohamed, I. Madaci, T. Tchelidze, M. Modreanu, P. Vales-Castro, C. Rubio, C. Arnold, V. Sallet, Y. Dumont, and A. Perez-Tomas, Enhancing the intrinsic p-type conductivity of the ultra-wide bandgap Ga_2O_3 semiconductor, J. Mater. Chem. C **7**, 10231 (2019).

[72] S. Poncé, M. Schlipf, and F. Giustino, Origin of low carrier mobilities in halide perovskites, ACS Energy Lett. **4**, 456 (2019).

[73] I.-T. Lu, J. Park, J. J. Zhou, and M. Bernardi, Ab initio electron-defect interactions using Wannier functions, npj Comput. Mater. **6**, 17 (2020).

[74] H. Brooks, Scattering by ionized impurities in semiconductors, Phys. Rev. **83**, 879 (1951).

[75] C. Herring, Transport properties of a many-valley semiconductor, Bell Sys. Tech. J. **34**, 237 (1955).

[76] S. S. Li and W. R. Thurber, The dopant density and temperature dependence of electron mobility and resistivity in n-doped silicon, Solid-State Electron. **20**, 609 (1977).

[77] S. Poncé, D. Jena, and F. Giustino, Hole mobility of strained GaN from first principles, Phys. Rev. B **100**, 085204 (2019).

[78] S. Poncé, D. Jena, and F. Giustino, Route to High Hole Mobility in GaN via Reversal of Crystal-Field Splitting, Phys. Rev. Lett. **123**, 096602 (2019).

[79] E. Johnson, Physical limitations on frequency and power parameters of transistors, RCA Rev. **13**, 27 (1965).

[80] R. W. Keyes, Figure of merit for semiconductors for high speed switches, Proc. IEEE **60**, 225 (1972).

[81] A. Fiedler, R. Schewski, Z. Galazka, and K. Irmscher, Static dielectric constant of β-Ga_2O_3 perpendicular to the principal

planes (100), (010), and (001), ECS J. Solid State Sci Technol. **8**, Q3083 (2019).

[82] K. Karch, T. Dietrich, W. Windl, P. Pavone, A. P. Mayer, and D. Strauch, Contribution of quantum and thermal fluctuations to the elastic moduli and dielectric constants of covalent semiconductors, Phys. Rev. B **53**, 7259 (1996).

[83] P. Norton, T. Braggins, and H. Levinstein, Impurity and lattice scattering parameters as determined from Hall and mobility analysis in *n*-type silicon, Phys. Rev. B **8**, 5632 (1973).

[84] C. Kim, G. Pilania, and R. Ramprasad, From organized high-throughput data to phenomenological theory using machine learning: The example of dielectric breakdown, Chem. Mater. **28**, 1304 (2016).

[85] P. Gorai, R. W. McKinney, N. M. Haegel, A. Zakutayev, and V. Stevanovic, A computational survey of semiconductors for power electronics, Energy Environ. Sci. **12**, 3338 (2019).

[86] Y. Sun, C. Bealing, S. Boggs, and R. Ramprasad, 50+ years of intrinsic breakdown, IEEE Electr. Insul. Mag. **29**, 8 (2013).

[87] K. Ghosh and U. Singisetti, Electron mobility in monoclinic β-Ga_2O_3—Effect of plasmon-phonon coupling, anisotropy, and confinement, J. Mater. Res. **32**, 4142 (2017).

[88] H. W. Icenogle, B. C. Platt, and W. L. Wolfe, Refractive indexes and temperature coefficients of germanium and silicon, Appl. Opt. **15**, 2348 (1976).